

Article

An Investigation into Microstructures and Mechanical Properties of 1060 Pure Aluminum during Submerged Friction Stir Processing at a High Rotating Speed

Yuchen Peng ¹, Qi Zhang ¹, Lingyou Wen ¹, Zonghua Xie ¹, Biao Huang ¹, Shanshan Hu ², Hongqun Tang ^{1,*} and Chunhua Wei ^{1,*}

- ¹ Guangxi Key Laboratory of Processing for Nonferrous Metals and Featured Materials, Center of Ecological Collaborative Innovation for Aluminum Industry in Guangxi, School of Resources, Environment and Materials, Guangxi University, Nanning 530004, China; p3315290449@163.com (Y.P.); 18855508609@163.com (Q.Z.); wly1141322492@163.com (L.W.); xzh19971031@163.com (Z.X.); 18717875318@163.com (B.H.)
- ² College of Mechanical Engineering, Guangxi University, Nanning 530004, China; hsswhh@gxu.edu.cn
- * Correspondence: hqtang@gxu.edu.cn (H.T.); 20150071@gxu.edu.cn (C.W.)

Abstract: In this work, 1060 pure aluminum was subjected to high rotating speed submerged friction stir processing (HRS-SFSP). The heat cycle curve of the processing area was measured by K-type thermocouple and temperature recorder. The microstructure, grain size, texture, and tensile fracture of the processing area were analyzed by electron backscattered diffraction and scanning electron microscopy. The results show that the HRS-SFSP caused severe plastic deformation of 1060 aluminum and produced fine recrystallized grains. The minimum average grain size was 0.686 μm at the 2-pass. In addition, the dislocation density in the stirred region was greatly reduced and the high angle grain boundaries (HAGBs) were dominant. The texture strength of pure aluminum increased with the increase in processing passes. The maximum hardness of 66.3 HV and ultimate tensile strength of 95.2 MPa were obtained at 1-pass, which were 86% and 33.9% higher than those of the base material, respectively. The hardness and strength of the stirring zone (SZ) decreased with the increase in the number of processing passes. Therefore, HRS-SFSP pure aluminum can obtain high strength and hardness while maintaining good plasticity.

Keywords: high rotating speed submerged friction stir processing; 1060 pure aluminum; microstructure; mechanical properties



Citation: Peng, Y.; Zhang, Q.; Wen, L.; Xie, Z.; Huang, B.; Hu, S.; Tang, H.; Wei, C. An Investigation into Microstructures and Mechanical Properties of 1060 Pure Aluminum during Submerged Friction Stir Processing at a High Rotating Speed. *Metals* **2022**, *12*, 201. <https://doi.org/10.3390/met12020201>

Academic Editor:
Menachem Bamberger

Received: 29 November 2021

Accepted: 17 January 2022

Published: 21 January 2022

Publisher's Note: MDPI stays neutral with regard to jurisdictional claims in published maps and institutional affiliations.



Copyright: © 2022 by the authors. Licensee MDPI, Basel, Switzerland. This article is an open access article distributed under the terms and conditions of the Creative Commons Attribution (CC BY) license (<https://creativecommons.org/licenses/by/4.0/>).

1. Introduction

Friction stir processing (FSP) is a new solid state processing technology, which was improved by R.S. Mishra et al. [1], as an improved technique based on friction stir welding (FSW). Its principle is similar to that of FSW, wherein a rotating tool with a pin and a shoulder acts on the surface of the material. The pin tool rotates at a high rotating speed and advances at a uniform rotating speed, resulting in severe plastic deformation in the nugget zone (NZ) as well as grain crushing and refinement, which greatly improves the performance of the base material. The NZ can be roughly divided into four areas [2,3]: the outermost unaffected base material (BM); the heat affected zone (HAZ), which is affected by heat but does not produce large plastic deformation; the stirring zone (SZ) of the stirring needle processing; and the thermo mechanical affected zone (TMAZ) between the HAZ and the SZ. At present, FSP and FSW have been used in the processing and welding of various aluminum alloys and copper alloys. Yadva and Bauri [4] conducted FSP on cast aluminum and found that the mechanical properties of cast aluminum were improved. Heinz et al. [5] reported that heat treatment after FSW could further improve the mechanical properties of 6013 aluminum alloy.

The rotating speed of the tool is always one of the main parameters that affect the performance of SZ. In the published literature, the stirring head speed of various materials in FSP is mostly based on a low rotating speed (200–2000 r/min), as shown in Figure 1 [6–25], and there are few studies on FSP at higher rotating speeds (≥ 3000 r/min). Scholars [26] believe that heat input in FSW and FSP processes can be reduced at a low rotating speed, so as to obtain better weld quality. However, at a low rotating speed, the welding machine has to overcome larger resistance to work owing to insufficient flow plasticity, which exerts greater pressure on the spindle and limits the application of FSP. Therefore, Azimzadegan [27] proposed that increasing the rotating speed can soften the processing area, improve the flow plasticity, and then reduce the stress on the spindle. However, Li et al. [28] pointed out that a high rotating speed would produce high heat input, which would be detrimental to the performance of welded joints. Abolusoro et al. [29] found that, at 1850 r/min, the welding temperature reached 550 °C, which seriously affected the weld performance. External cooling is a method to improve the microstructure and properties during welding. Providing a water environment in the process can quickly reduce the temperature of the BM, effectively inhibit the growth of recrystallized grains, obtain a fine recrystallized structure, and improve the performance of the material. Su [30] found that providing a water environment in the process of FSP can take away the remaining heat in a timely manner and inhibit the recrystallization and growth of refined grains, while improving the strength and plasticity of materials.

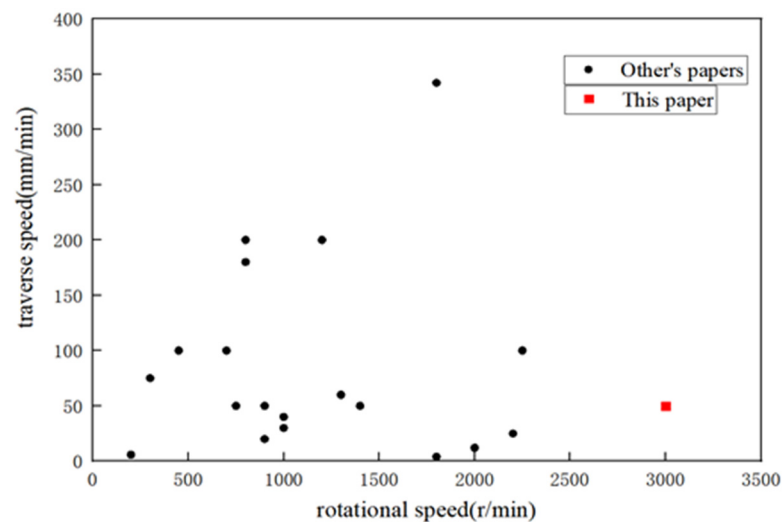


Figure 1. Black dots represent previously published parameters and red squares represent parameters of this study.

Therefore, the concept of high rotating speed submerged friction stir processing (HRS-SFSP) is proposed in this paper. In order to understand the effect of HRS-SFSP on the microstructure and properties of an aluminum matrix, 1060 pure aluminum was used as the matrix material in this study.

2. Materials and Methods

The base material used in this study is 1060 industrial pure Al with 99.6% Al, Si, and Cu content of less than 0.4%. First, 1060 pure aluminum was rolled into a 3 mm thick sheet metal for 1, 2, and 3 passes of reciprocating FSP. Then, a 2 mm pin tool with a top diameter of 3.5 mm and a tip diameter of 2.5 mm with a shoulder diameter of 10 mm was used for the FSP. The rotating speed was kept constant at 3000 r/min, the travelling speed was fixed at 60 mm/min, and the downward pressure was 0.2 mm. The whole process was carried out under cold water, the water flow speed is about 300 mm/s, and the direction is opposite to the processing direction. A K-type thermocouple was inserted in a position about 1.5 mm away from each NZ, and the temperature recorder was used to record the

temperature at two points per second to obtain the heat cycle curve. Before processing, the surface of the Al sheet was polished with sandpaper and cleaned with alcohol to remove oxides and impurities.

After the experiment, samples with a size of $20 \text{ mm} \times 10 \text{ mm} \times 3 \text{ mm}$ were collected along the machining surface. The samples were mechanically ground and electrolytically polishing in $-20 \text{ }^\circ\text{C}$ alcohol perchlorate solution (1:9) for 15 s at a voltage of 30 V. The microstructures were analyzed using electron backscattered diffraction (EBSD) technology with a scanning step of $0.05 \text{ }\mu\text{m}$. More than 700 grains were counted for each sample using Channel 5 software and the following standard definitions were adopted: θ_c represents the difference of orientation angle between neighboring grains and $\theta_c = 2^\circ$ is defined as the boundary of sub-grains. When θ_c is greater than 2° , it is considered that the grain degenerates, and $\theta_c = 15^\circ$ is used as the boundary between high angle grain boundaries (HAGBs) and low angle grain boundaries (LAGBs). Average grain size, poor orientation of adjacent grains, dislocation, and Schmidt factor were analyzed. The hardness was tested by (HCT-1000) micro-Vickers hardness tester. The applied load was 4 N, the pressure holding time was 15 s, the hardness was collected from the advancing side (AS) to the retreating side (RS) at a point every 0.5 mm downward along the cross section, and the hardness distribution in the NZ was obtained. Tensile test was carried out using Zwick/Z2.5 (Zwick, Ulm, Germany). Three groups were tested for each parameter, and the fracture morphology was observed by scanning electron microscopy (SEM). Tensile specimens were taken from the parallel processing direction, as shown in Figure 2a. Figure 2b shows the size of the tensile specimens. Figure 2c presents the FSP morphology, while Figure 2d shows the optical microstructure of the cross section.

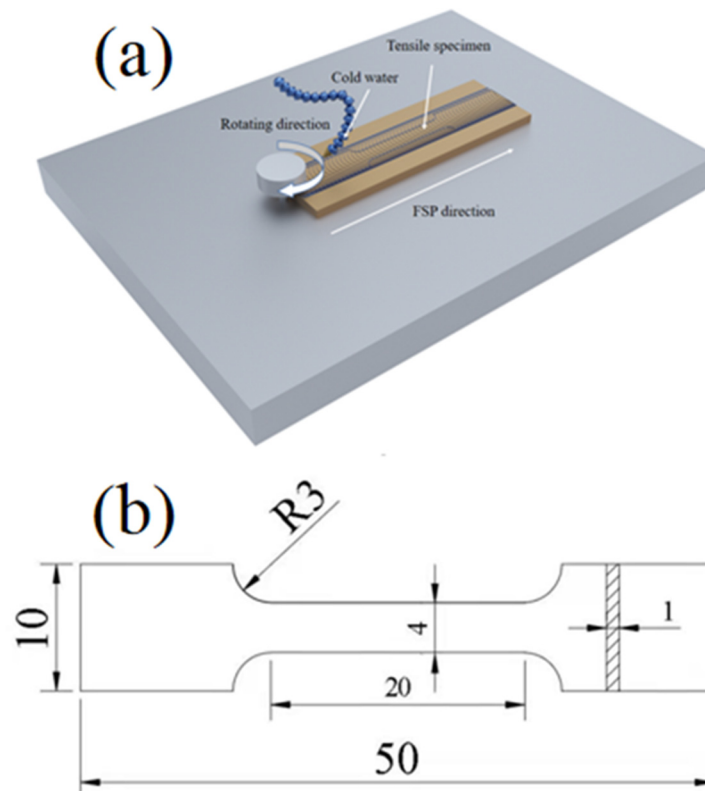


Figure 2. Cont.

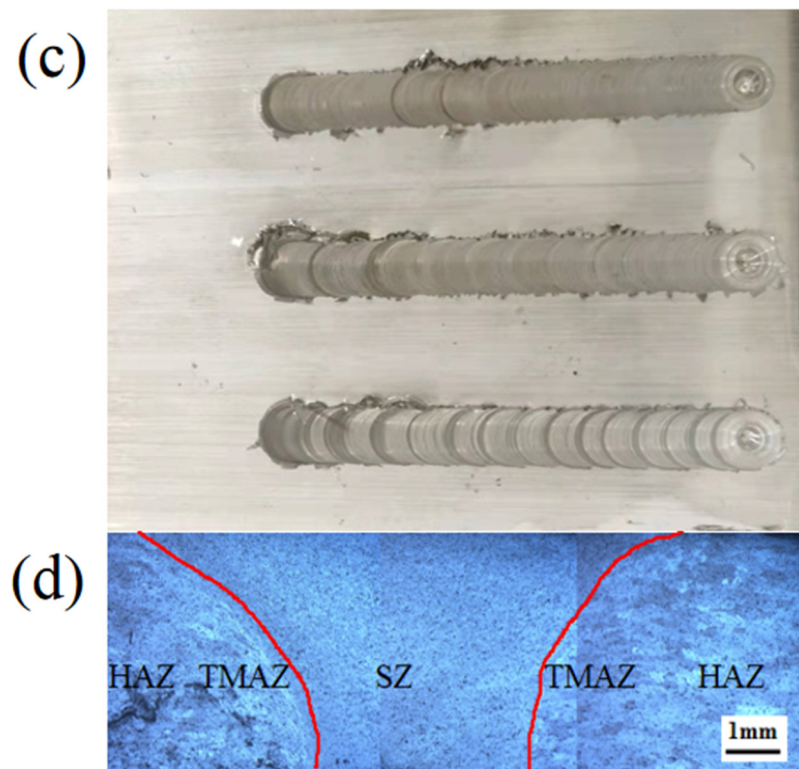


Figure 2. (a) Schematic diagram of HRS-SFSP and sampling location. (b) Tensile specimens' size (c) HRS-SFSP morphology. (d) Optical microstructure of the cross section.

3. Results and Discussion

3.1. Thermal Cycle Curve

Figure 3 shows the distribution curve of thermal cycle in the processing area under different passes. It can be seen that the peak temperature of the processing area reached $0.65 T_m$ – $0.71 T_m$ (T_m is the melting point of the material) after 1–3 pass of FSP of pure aluminum. These temperatures are far lower than the melting point of aluminum (~ 660 °C) and higher than the recrystallization temperature of aluminum ($0.4 T_m$ – $0.5 T_m$). This indicates that dynamic recrystallization has occurred in the SZ. The temperature of the processing zone can be expressed as follows [31]:

$$T = K \left(\frac{\omega^2}{v \times 10^4} \right)^\alpha \times T_m \quad (1)$$

where ω is the rotating speed; v is the travelling speed; and both α and K are constant, ranging from 0.04 to 0.06 and 0.65 to 0.75, respectively. According to Equation (1), large heat input can be obtained at a high rotating speed. The temperature of 2 and 3 passes is higher than 1-pass, as show here. This is because the process is continuous. The heat generated did not completely disappear before the next processing pass, which caused heat accumulation. Consequently, the temperature continued to rise during the subsequent processing. The water cooling caused a rapid decline in the temperature of the processing area. Finally, the temperature distribution as shown in Figure 3 was formed.

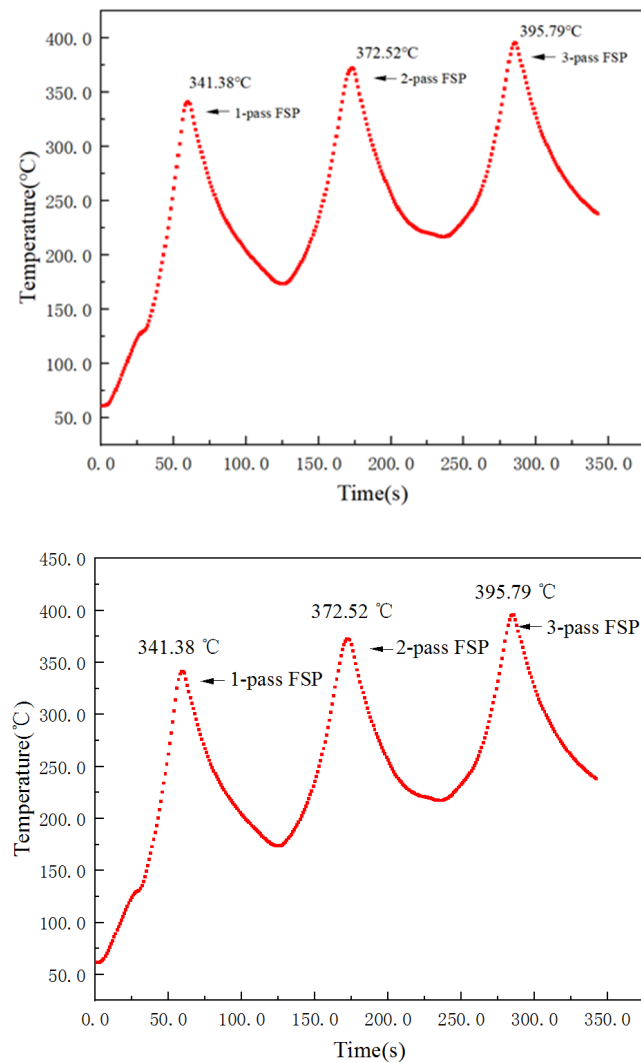


Figure 3. Thermal cycle curves of the advancing side with different passes processing.

3.2. Microstructure Characterization

Figure 4 shows the inverse pole figure (IPF) on the AS of 1–3 passes. It can be seen that small, recrystallized grains were obtained in SZ after HRS-SFSP. Combined with Figure 5, it can be seen that ultrafine-grains with an average grain size of $0.690\ \mu\text{m}$ and $0.686\ \mu\text{m}$ were obtained at 1 and 2 passes, respectively. However, with the increase in number of processing passes, the grains in SZ began to coarsen and reached $5.363\ \mu\text{m}$ at 3-pass. The analysis shows that, on the one hand, multi-pass processing can further break the grains and help refine the grains again. On the other hand, temperature also significantly affects the recrystallization grain size in the SZ. Excessive heat input led to the continuous rise in the temperature in the SZ, as shown in Figure 3, which resulted in the growth and coarsening of the refined grains in the SZ. This explains why the average grain size of 1 and 2 passes was similar, and the average grain size of 3-pass was larger than that of 2-pass. The ultrafine-grains were still obtained at a high rotating speed owing to the cooling effect of water, which effectively inhibited the continuous growth of recrystallized grains. Hence, fine recrystallized grains were obtained.

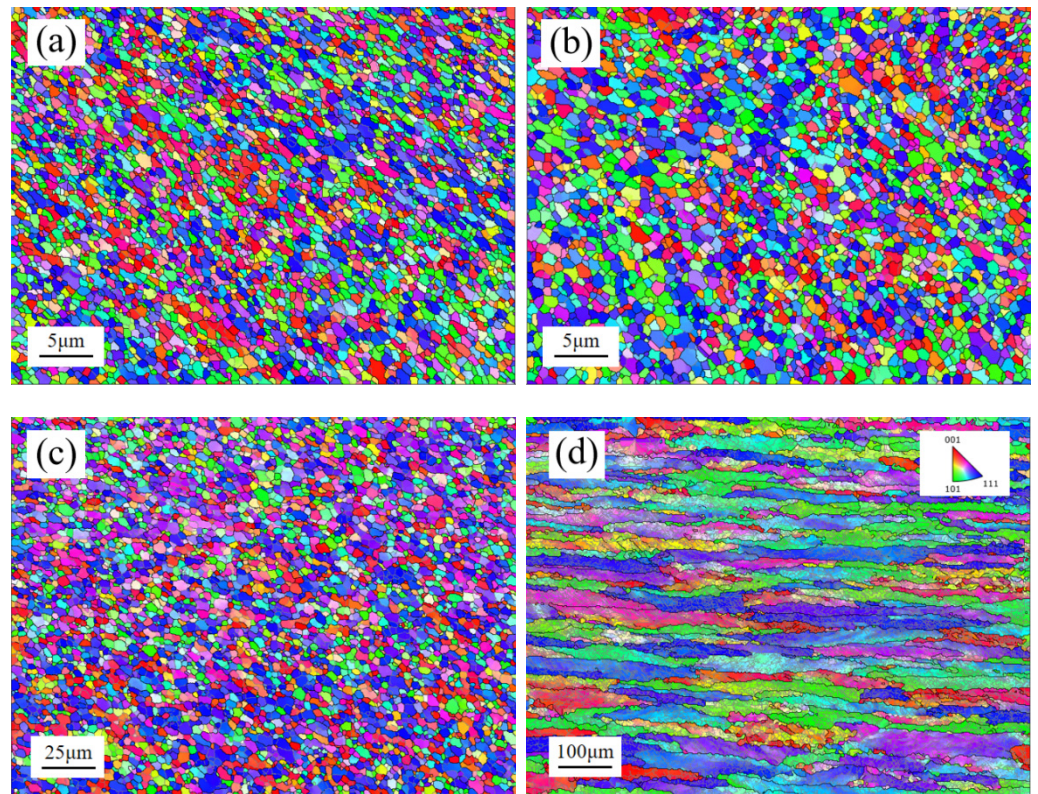


Figure 4. IPF on the AS. (a) 1-pass FSP; (b) 2-pass FSP; (c) 3-pass FSP; (d) BM.

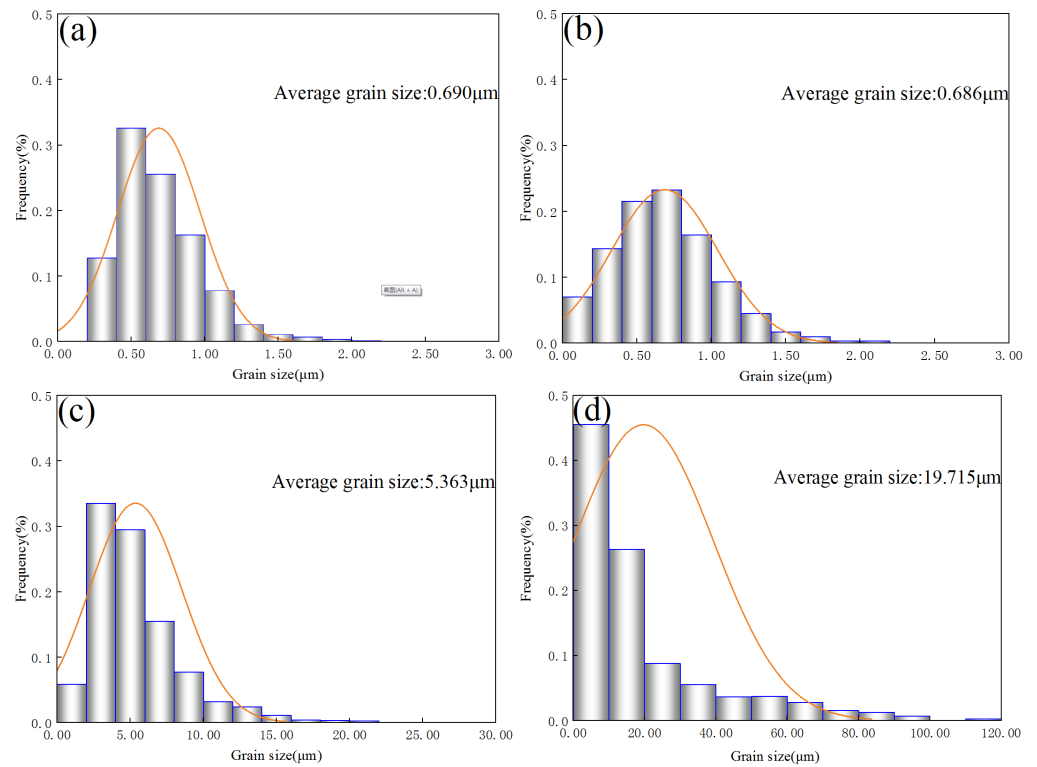


Figure 5. Average grain size on the AS. (a) 1-pass FSP; (b) 2-pass FSP; (c) 3-pass FSP; (d) BM.

Figure 6 shows the results of misorientation angle on the AS. It can be seen that the HRS-SFSP generated more HAGBs, which made crack propagation difficult, thus improving the toughness of the material. There was a high proportion (>85%) of HAGBs after 1 and

2 passes, as shown in Figure 5a,b, which is different from the results of other severe plastic deformation (SPD) and ordinary rotating speed FSP. SPD techniques such as equal channel angular extrusion (ECAE) and equal channel angular expansion extrusion with spherical cavity (ECAEE-SC) [32] produce mostly LAGBs, thus a large number of HAGBs should be formed by means of recovery recrystallization annealing to improve the toughness. More HAGBs can also be obtained by ordinary rotating speed FSP. Liu et al. [18] carried out FSP on 1050 pure aluminum at a speed of 1200 r/min and obtained 70–80% HAGBs on the forward side, which was lower than that obtained by HRS-SFSP. According to the analysis, a high rotating speed causes greater plastic deformation and strain rate. Under such conditions, more LAGBs were transformed into HAGBs by absorbing dislocation, that is, more complete “continuous dynamic recrystallization” [33] occurred, thus forming a large number of HAGBs. At the same time, as a result of water cooling, the growth of recrystallization was inhibited, which prevented the HAGBs from changing back to LAGBs. Finally, a large proportion of HAGBs were obtained. However, the 3-pass processing zone experienced a high thermal cycle, so static recrystallization occurred in the subsequent process, and some HAGBs were converted to LAGBs again, resulting in a significant decrease in the proportion of HAGBs. In general, SPD and low rotating speed FSP require multiple post-processing methods or require multiple passes to obtain a large number of HAGBs, while with HRS-SFSP, more HAGBs can be obtained in fewer passes.

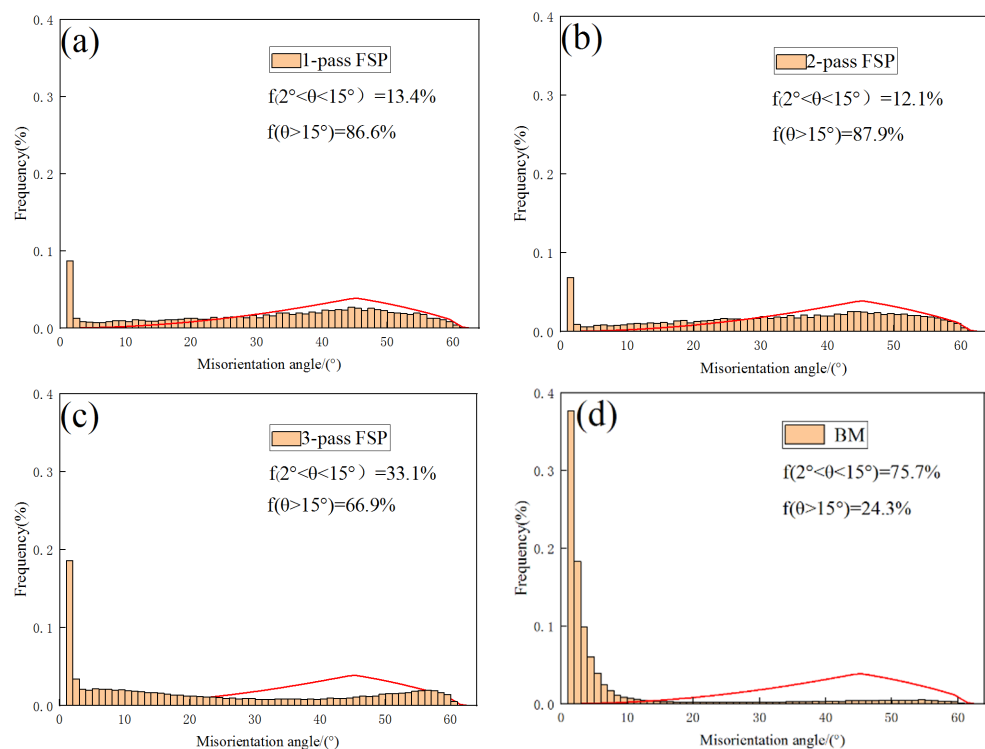


Figure 6. Misorientation angle on the AS. (a) 1-pass FSP; (b) 2-pass FSP; (c) 3-pass FSP; (d) BM.

In order to better understand the mechanical properties (hardness and tensile strength) of 1060 pure aluminum, it is necessary to consider grain size, dislocation density, and slip system. Among them, grain size and dislocation density are important factors affecting hardness and strength, while Schmid factor (SF) is an important parameter describing the slip system. Thus, the two parameters of geometrically necessary dislocation (GND) density and SF were used to quantitatively analyze strength and plasticity. Grain size information is given in Figures 3 and 4. GND density information is obtained using the following formula [34]:

$$\rho^{GND} = \frac{2\Delta\theta_i}{ub} \quad (2)$$

where $\Delta\theta_i$ means local misorientation kernel average misorientation, as shown in Figure 7; u is the unit point length (step size); and b is the burgers vector. For pure aluminum, the step size is $0.05\ \mu\text{m}$ and b is $0.286\ \text{nm}$ [35] (which was explained in the experimental part). The GND density can be obtained by substituting it into Equation (2), as shown in Figure 8. It can be seen that the geometric dislocation density (GND) of 1–3 passes must be much lower than BM, which was the result of recrystallization. The dislocation density of 3-pass was the minimum because the thermal cycle time of 3-pass was the longest and the grain grows, leading to the decrease in GND density.

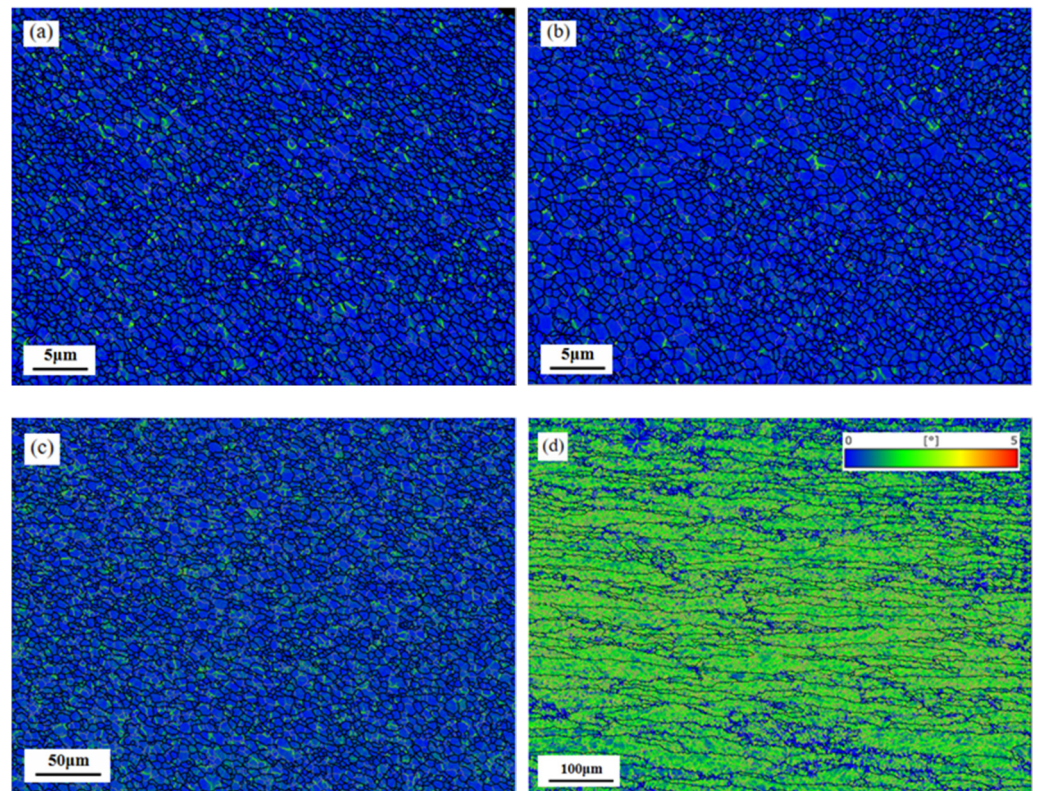


Figure 7. Kernel average misorientation of the AS. (a) 1 pass FSP; (b) 2-pass FSP; (c) 3-pass FSP; (d) BM.

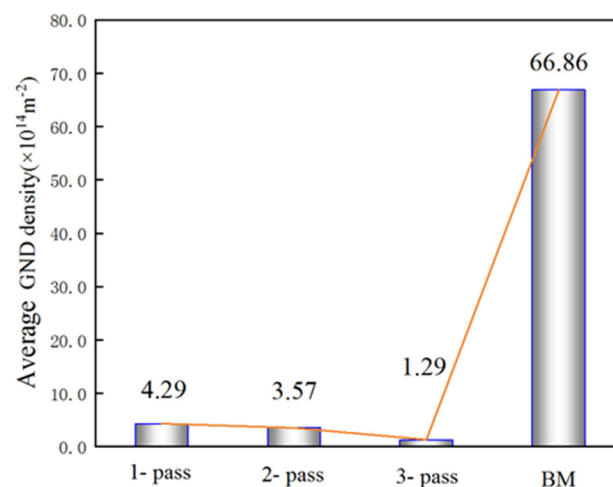


Figure 8. GND density distribution on the AS.

SF can reflect the plasticity of the material, as shown in Figure 9. With the increase in number of processing passes, SF gradually increases. It can be considered that the increase in the number of processing passes cannot always improve the mechanical properties

of the material. During HRS-SFSP, the plasticity of the processing area showed a large improvement at the time of 3-pass, which indicates that the plasticity of the processing area will improve at the time of 3-pass, which is unfavorable to the mechanical properties of the processing area.

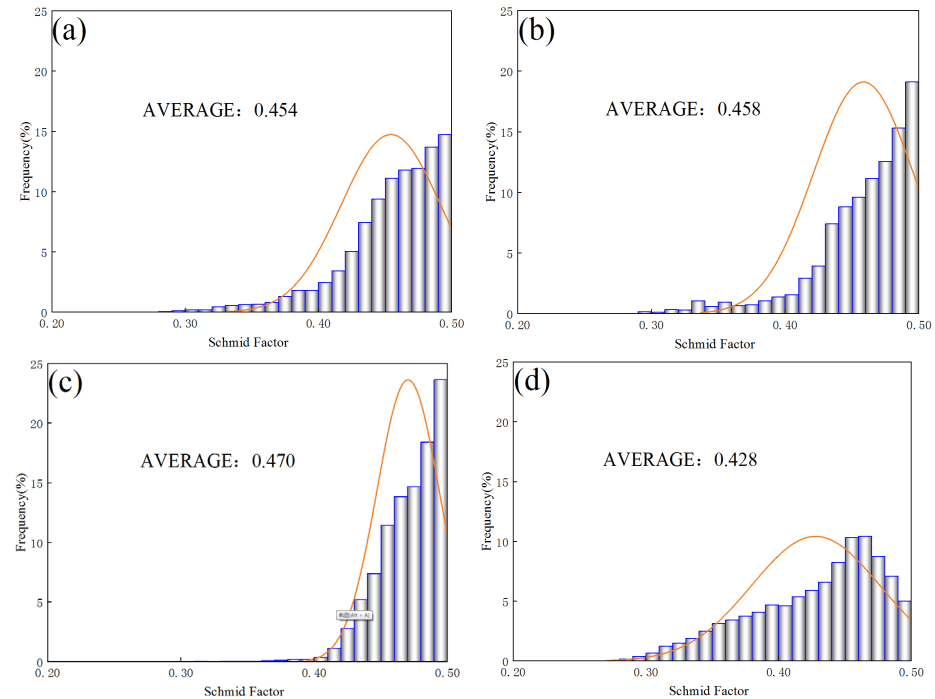


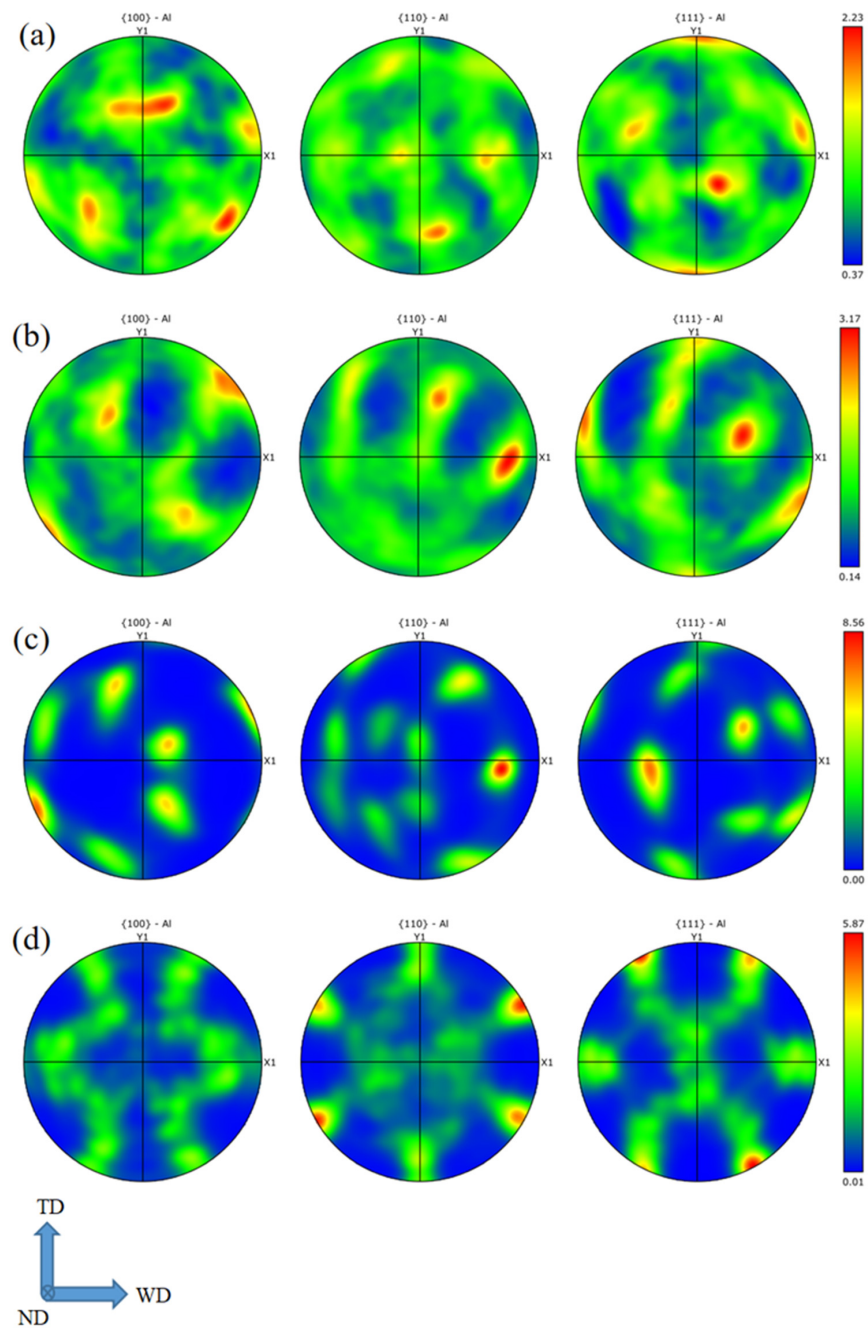
Figure 9. $\{111\}\langle 110\rangle$ distribution of SF. (a) 1-pass FSP; (b) 2-pass FSP; (c) 3-pass FSP; (d) BM.

3.3. Texture Characterization

Table 1 lists the main texture of 1060 aluminum BM and the AS of 1–3 passes processing. Copper texture, goss texture, and cube texture are mainly found in BM. However, after HRS-SFSP, the texture types and contents changed. Specifically, the content of copper texture decreased greatly, while the shearing texture and cube texture were the main textures, and their content showed an increasing trend. Combined with the polar graph of Figure 10, it can be seen that the texture strength at 1-pass was weak. With the increase in processing passes, the texture strength gradually increases, showing a new preferred orientation. At 3-pass, the relative content of shearing texture is up to 30.8%. According to the analysis, as aluminum is an FCC metal, the orientation factor in the $\langle 110\rangle$ direction of $\{111\}$ plane is the smallest during plastic deformation [36]. The high rotating speed stirring needle leads to large shear deformation, which leads to the dislocation in the grains to form $\{111\}\langle 110\rangle$ orientation, that is, dynamic recrystallization. However, the temperature of HRS-SFSP was higher than the recrystallization temperature of aluminum. This resulted in the dynamic recovery of cube texture sub-grains in the SZ under the action of thermal cycling, and then the recrystallization growth occurred, namely, “discontinuous dynamic recrystallization” [37]. Finally, shearing texture and cube texture were formed.

Table 1. Main texture types and contents.

Texture Types	BM	1-Pass FSP	2-Pass FSP	3-Pass FSP
Cube {001}<100>	4.66%	6.48%	3.29%	7.26%
Rotating cubic {001}<110>	1.07%	3.28%	3.83%	2.28%
Copper {112}<111>	7.91%	5.02%	1.83%	0.39%
Brass {011}<211>	0.22%	5.93%	9.16%	1.22%
R {124}<211>	0.62%	5.42%	2.49%	<0.01%
Shearing {111}<110>	0.11%	7.48%	19.1%	30.8%
Goss {011}<100>	4.51%	2.95%	5.77%	2.73%

**Figure 10.** Polar figure (a) 1-pass FSP; (b) 2-pass FSP; (c) 3-pass FSP; (d) BM.

3.4. Hardness

Hardness is one of the important mechanical properties to measure the ability of material to resist deformation caused by external force. The average Vickers hardness of 1060 pure aluminum used in this paper was 35.6 HV. Figure 11 shows the hardness distribution of 1–3 pass processing. At 1 and 2 passes, “M” type hardness distribution was observed, while “U” type hardness distribution was observed at 3-pass. Gan [10] et al. reported that the hardness distribution of pure aluminum presented a “U” type trend after low rotating speed FSP, and the hardness of SZ was lower than that of BM. However, the increase in hardness came from fine grains and high GND density after HRS-SFSP. However, with the increase in the number of processing passes, the recrystallized grains grew by consuming GND density, resulting in the decrease in GND density and growth of grain size, and finally the decrease in hardness. In conclusion, the highest average micro-hardness was obtained in SZ at 1-pass, reaching 66.3 HV, which was about 86% higher than that of the BM. In contrast, at 3-pass, the average hardness of SZ decreases to 32.6 HV, which was lower than that of the BM.

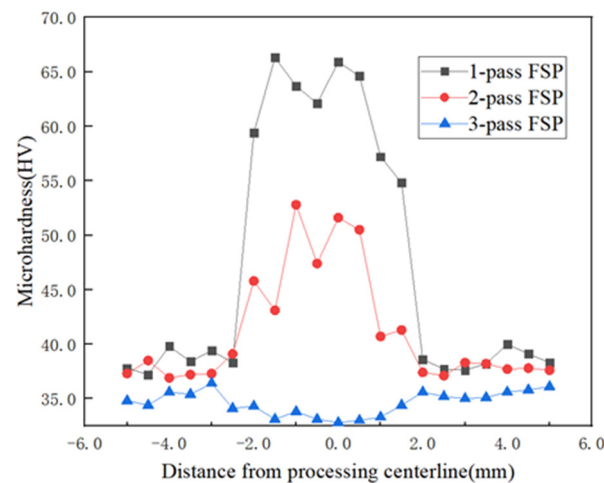


Figure 11. Hardness distribution of different passes.

3.5. Ultimate Tensile Strength

Figure 12 shows the ultimate tensile strength and elongation under various parameters. It can be seen that the ultimate tensile strength showed a downward trend with the increase in the number of processing passes. The maximum ultimate tensile strength of 95.2 MPa was obtained at 1-pass, which can be explained by the classical hall–page relationship. The grain size at 1 and 2 passes was refined to submicron level, so the ultimate tensile strength increased greatly. Although the strength of 3-pass is still higher than that of the BM, the grain size of 3-pass was significantly larger than that of 1- and 2-passes, resulting in the reduction of ultimate tensile strength. Figure 13 shows the tensile fracture morphology of the BM and 1–3 passes. It can be seen that there were large dimples and cleavage surfaces in the fracture of BM, and mixed fracture occurred. In contrast, there were only dimples after 1–3 passes, which was a typical ductile fracture. Moreover, the dimples of 3-pass were smaller and deeper than those of 1- and 2-passes samples, indicating that the processed metal after 3-pass had better plasticity, which was also consistent with the variation trend of elongation reflected in Figure 5. The analysis shows that the long duration of multi-pass processing led to heat accumulation. Under the action of thermal cycle, static recrystallization of SZ occurred after processing. This causes the HAGBs to gradually change into LAGBs, resulting in the increase in texture strength. At the same time, the SF also increased accordingly, which improves the slip ability of SZ. Therefore, SZ shows good plasticity under the action of external force. These findings provide a theoretical basis for the future application of multi-pass HRS-SFSP in alloys and composites.

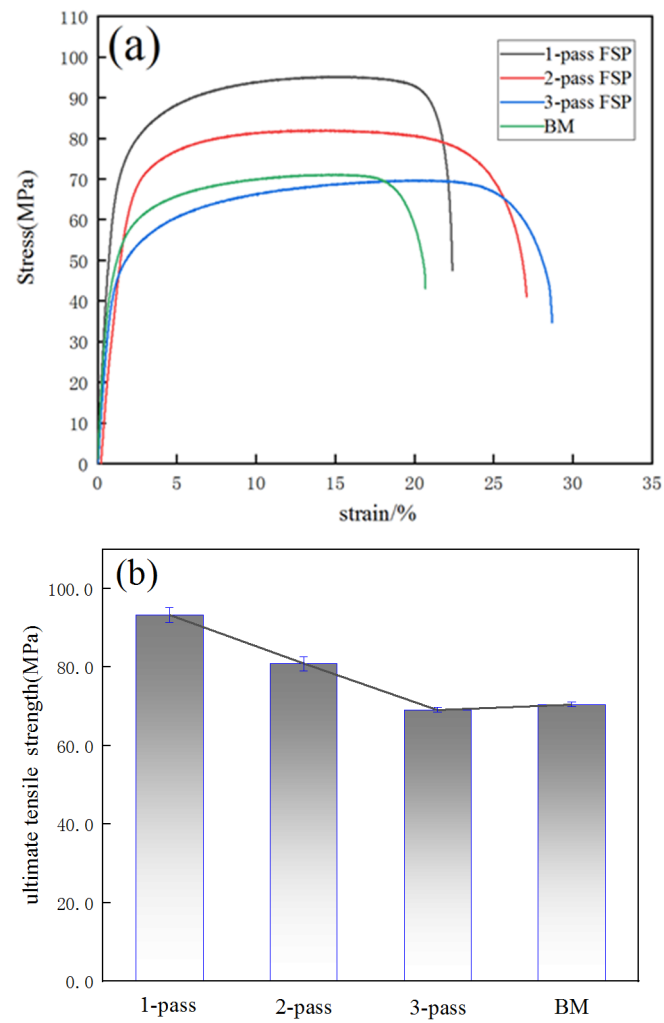


Figure 12. 1–3 passes tensile. (a) True stress–strain curve; (b) ultimate tensile strength.

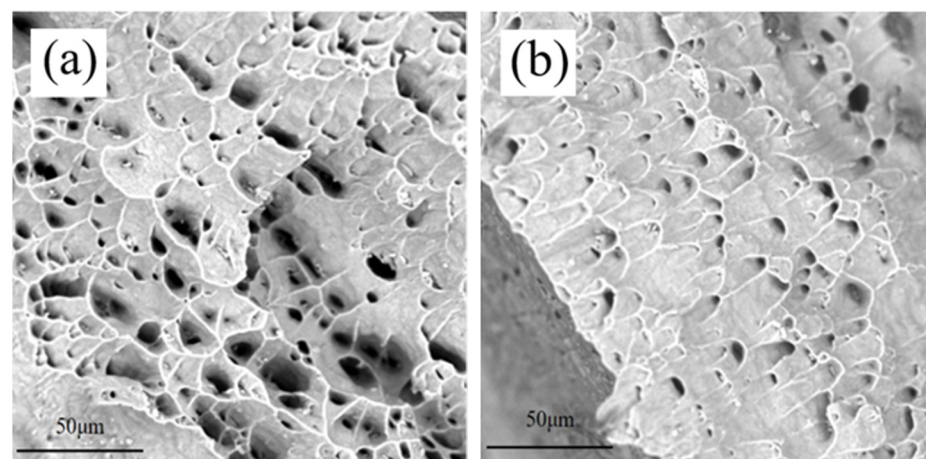


Figure 13. Cont.

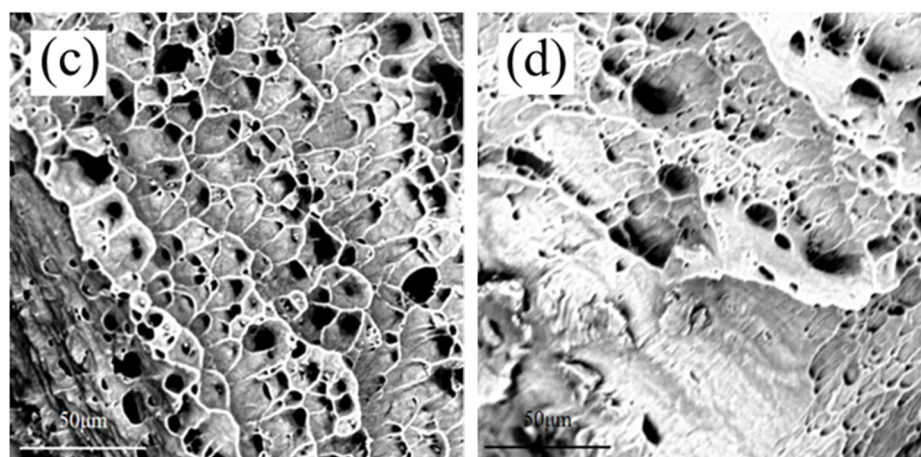


Figure 13. Fracture morphology. (a) 1-pass FSP; (b) 2-pass FSP; (c) 3-pass FSP; (d) BM.

4. Conclusions

- (1) Fine and evenly distributed recrystallized grains of 1060 pure aluminum can be obtained after multi-pass HRS-SFSP. With the increase in processing passes, the grain size increases significantly.
- (2) HRS-SFSP of 1060 pure aluminum includes three processes: continuous dynamic recrystallization, discontinuous dynamic recrystallization, and static recrystallization. The proportion of HAGBs and LAGBs reflects the degree of recrystallization in each pass. The highest proportion of HAGBs was obtained after 1-pass processing, depending on the degree of dynamic recrystallization.
- (3) With the increase in the number of processing passes, the elongation increased gradually, while the strength and hardness decreased. After 3-pass, the hardness was even lower than that of the BM. These results show that, during HRS-SFSP, fewer passes are conducive to the improvement in strength and hardness, while more passes are conducive to the improvement in plasticity.

Author Contributions: Conceptualization, Y.P. and H.T.; methodology, L.W. and Y.P.; validation, Y.P., Q.Z., and S.H.; investigation, Q.Z. and Z.X.; resources, Y.P.; data curation, H.T.; writing—original draft preparation, Y.P. and L.W.; writing—review and editing, Y.P. and Z.X.; visualization, Q.Z.; supervision, B.H. and C.W.; project administration, H.T.; funding acquisition, H.T., S.H., and C.W. All authors have read and agreed to the published version of the manuscript.

Funding: This research was funded by National Natural Science Foundation of China (51965005), Key Projects of Regional Innovative Cooperative Development Foundation from NSFC (U20A20276), The Natural Science Foundation of Guangxi (2018GXNSFAA281258), Science and Technology Major Project of Nanning, Guangxi (20211004), and Guangxi Education Postgraduate Innovation Program in 2022 (No.72).

Informed Consent Statement: Not applicable.

Data Availability Statement: Not applicable.

Conflicts of Interest: The authors declare no conflict of interest.

References

1. Mishra, R.S.; Mahoney, M.W.; McFaden, S.X.; Mara, N.A.; Mukherjee, A.K. High strain rate superplasticity in a friction stir processed 7075 Al alloy. *Scr. Mater.* **1999**, *42*, 163–168. [[CrossRef](#)]
2. Murr, L.E.; Ying, L.; Flores, R.D.; Trillo, E.A.; Mcclure, J.C. Intercalation vortices and related microstructural features in the friction-stir welding of dissimilar metals. *Mater. Res. Innov.* **1998**, *2*, 150–163. [[CrossRef](#)]
3. Benavides, S.; Li, Y.; Murr, L.E.; Brown, D.; Mcclure, J.C. Low-temperature friction-stir welding of 2024 aluminum. *Scr. Mater.* **1999**, *41*, 809–815. [[CrossRef](#)]
4. Yadav, D.; Bauri, R. Effect of friction stir processing on microstructure and mechanical properties of aluminium. *Mater. Sci. Eng. A* **2012**, *539*, 85–92. [[CrossRef](#)]

5. Heinz, B.; Skrotzki, B. Characterization of a friction-stir-welded aluminum alloy 6013. *Metall. Mater. Trans. B* **2002**, *33*, 489–498. [[CrossRef](#)]
6. Reynolds, A.P.; Hood, E.; Wei, T. Texture in friction stir welds of Timetal 21S. *Scr. Mater.* **2005**, *52*, 491–494. [[CrossRef](#)]
7. Mahmoud, E.R.I.; Takahashi, M.; Shibayanagi, T.; Ikeuchi, K. Effect of friction stir processing tool probe on fabrication of SiC particle reinforced composite on aluminium surface. *Sci. Technol. Weld. Join.* **2009**, *14*, 413–425. [[CrossRef](#)]
8. Han, M.-S.; Lee, S.-J.; Park, J.-C.; Ko, S.-C.; Woo, Y.-B.; Kim, S.-J. Optimum condition by mechanical characteristic evaluation in friction stir welding for 5083-O Al alloy. *Trans. Nonferrous Met. Soc. China* **2009**, *19* (Suppl. 1), s17–s22. [[CrossRef](#)]
9. Kurt, A.; Uygur, I.; Cete, E. Surface modification of aluminium by friction stir processing. *J. Mater. Processing Technol.* **2011**, *211*, 313–317. [[CrossRef](#)]
10. Gan, W.Y.; Zhou, Z.; Zhang, H.; Peng, T. Evolution of microstructure and hardness of aluminum after friction stir processing. *Trans. Nonferrous Met. Soc. China* **2014**, *24*, 975–981. [[CrossRef](#)]
11. Chen, Y.; Ding, H.; Ji-Zhong, L.I.; Zhao, J.W.; Ming-Jie, F.U.; Xiao-Hua, L.I. Effect of welding heat input and post-welded heat treatment on hardness of stir zone for friction stir-welded 2024-T3 aluminum alloy. *Trans. Nonferrous Met. Soc. China* **2015**, *25*, 2524–2532. [[CrossRef](#)]
12. Khan, N.Z.; Siddiquee, A.N.; Khan, Z.A.; Shihab, S.K. Investigations on tunneling and kissing bond defects in FSW joints for dissimilar aluminum alloys. *J. Alloy. Compd.* **2015**, *648*, 360–367. [[CrossRef](#)]
13. Khalilabad, M.M.; Zedan, Y.; Texier, D.; Jahazi, M.; Bocher, P. Effect of tool geometry and welding speed on mechanical properties of dissimilar AA2198-AA2024 FSWed joint. *J. Manuf. Processes* **2018**, *34*, 86–95. [[CrossRef](#)]
14. Sharma, A.; Sharma, V.M.; Paul, J. A comparative study on microstructural evolution and surface properties of graphene/CNT reinforced Al6061SiC hybrid surface composite fabricated via friction stir processing—ScienceDirect. *Trans. Nonferrous Met. Soc. China* **2019**, *29*, 2005–2026. [[CrossRef](#)]
15. Bikkina, V.; Talasila, S.R.; Adepu, K. Characterization of aluminum based functionally graded composites developed via friction stir processing. *Trans. Nonferrous Met. Soc. China* **2020**, *30*, 1743–1755. [[CrossRef](#)]
16. Butola, R.; Murtaza, Q.; Singari, R.M. Formation of Self-Assembled Monolayer and Characterization of AA7075-T6/B4C Nanoceramic surface composite using Friction Stir Processing. *Surf. Topogr. Metrol. Prop.* **2020**, *8*, 025030. [[CrossRef](#)]
17. Farghadani, M.; Karimzadeh, F.; Enayati, M.H.; Naghshehkish, N.; Moghaddam, A.O. Fabrication of AZ91D/Cu/Mg2Cu and AZ91D/Mg2Cu/MgCu2/MgO In-situ Hybrid Surface Nanocomposites via Friction Stir Processing. *Surf. Topogr. Metrol. Prop.* **2020**, *8*, 045002. [[CrossRef](#)]
18. Liu, X.C.; Zhen, Y.Q.; Sun, Y.F.; Shen, Z.K.; Wen-Ya, L.I. Local inhomogeneity of mechanical properties in stir zone of friction stir welded AA1050 aluminum alloy. *Trans. Nonferrous Met. Soc. China* **2020**, *30*, 2369–2380. [[CrossRef](#)]
19. Moaref, A.; Rabiezadeh, A. Microstructural evaluation and tribological properties of underwater friction stir processed CP-copper and its alloy. *Trans. Nonferrous Met. Soc. China* **2020**, *30*, 972–981. [[CrossRef](#)]
20. Li, J.; Zhao, M.; Jin, L.; Wang, F.; Dong, J. Simultaneously improving strength and ductility through laminate structure design in Mg–8.0Gd–3.0Y–0.5Zr alloys. *J. Mater. Sci. Technol.* **2021**, *71*, 195–200. [[CrossRef](#)]
21. Montes-González, F.A.; Rodríguez-Rosales, N.A.; Ortiz-Cuellar, J.C.; Muiz-Valdez, C.R.; Gómez-Casas, O. Experimental Analysis and Mathematical Model of FSW Parameter Effects on the Corrosion Rate of Al 6061-T6-Cu C11000 Joints. *Crystals* **2021**, *11*, 294. [[CrossRef](#)]
22. Regev, M.; Spigarelli, S. A Study of the Metallurgical and Mechanical Properties of Friction-Stir-Processed Cu. *Metals* **2021**, *11*, 656. [[CrossRef](#)]
23. Taghiabadi, R.; Jalali, H. Quality Index Assessment of Multi-Pass Friction Stir Processed Al–Si–Mg Alloys Fully Produced by Recycling of Machining Chips. *Trans. Indian Inst. Met.* **2021**, *74*, 273–284. [[CrossRef](#)]
24. Yu, X.; Wu, H.; Gong, W. Evaluating the Microstructure Evolution and Wear Behavior of Friction stir processed Aluminum Matrix Surface Composites with nano-sized SiC particles. *Surf. Topogr. Metrol. Prop.* **2021**, *9*, 015028. [[CrossRef](#)]
25. Zhou, L.; Ming-Run, Y.U.; Chen, W.G.; Zhang, Z.L.; Gao, F.Y. Microstructure and mechanical properties of friction stir processed TA5 alloy. *Trans. Nonferrous Met. Soc. China* **2021**, *31*, 404–415. [[CrossRef](#)]
26. Nan, X.; Song, Q.; Bao, Y.; Jiang, Y.; Shen, J. Achieving good strength-ductility synergy of friction stir welded Cu joint by using large load with extremely low welding speed and rotation rate. *Mater. Sci. Eng. A* **2017**, *687*, 73–81.
27. Azimzadegan, T.; Serajzadeh, S. An Investigation into Microstructures and Mechanical Properties of AA7075-T6 during Friction Stir Welding at Relatively High Rotational Speeds. *J. Mater. Eng. Perform.* **2010**, *19*, 1256–1263. [[CrossRef](#)]
28. Li, J.Q.; Liu, H.J. Effects of tool rotation speed on microstructures and mechanical properties of AA2219-T6 welded by the external non-rotational shoulder assisted friction stir welding. *Mater. Des.* **2013**, *43*, 299–306. [[CrossRef](#)]
29. Abolusoro, O.P.; Akinlabi, E.T.; Kailas, S.V. Tool rotational speed impact on temperature variations, mechanical properties and microstructure of friction stir welding of dissimilar high-strength aluminium alloys. *J. Braz. Soc. Mech. Sci. Eng.* **2020**, *42*, 176. [[CrossRef](#)]
30. Su, J.Q.; Nelson, T.W.; Sterling, C.J. Friction stir processing of large-area bulk UFG aluminum alloys. *Scr. Mater.* **2005**, *52*, 135–140. [[CrossRef](#)]
31. Commin, L.; Dumont, M.; Masse, J.-E.; Barrallier, L. Friction stir welding of AZ31 magnesium alloy rolled sheets: Influence of processing parameters. *Acta Mater.* **2009**, *57*, 326–334. [[CrossRef](#)]

32. Wang, X.X.; Zhang, X.; Jing, X.Y.; Yuan, J.C.; Song, W. Severe plastic deformation of commercially pure aluminum using novel equal channel angular expansion extrusion with spherical cavity. *Trans. Nonferrous Met. Soc. China* **2020**, *30*, 2613–2624. [[CrossRef](#)]
33. Huang, K.; Log, R.E. A review of dynamic recrystallization phenomena in metallic materials. *Mater. Des.* **2016**, *111*, 548–574. [[CrossRef](#)]
34. Yan, Z.; Wang, D.; He, X.; Wang, W.; Zhang, H.; Dong, P.; Li, C.; Li, Y.; Zhou, J.; Liu, Z.; et al. Deformation behaviors and cyclic strength assessment of AZ31B magnesium alloy based on steady ratcheting effect. *Mater. Sci. Eng. A Struct. Mater. Prop. Microstructure Processing* **2018**, *723*, 212–220. [[CrossRef](#)]
35. Kamikawa, N.; Hirochi, T.; Furuhashi, T. Strengthening Mechanisms in Ultrafine-Grained and Sub-grained High-Purity Aluminum. *Metall. Mater. Trans. A* **2018**, *50*, 234–248. [[CrossRef](#)]
36. Canova, G.R.; Kocks, U.F.; Jonas, J.J. Theory of torsion texture development. *Acta Metall.* **1984**, *32*, 211–226. [[CrossRef](#)]
37. Mcnelley, T.R.; Swaminathan, S.; Su, J.Q. Recrystallization mechanisms during friction stir welding/processing of aluminum alloys. *Scr. Mater.* **2008**, *58*, 349–354. [[CrossRef](#)]